JOURNAL OF GEOPHYSICAL RESEARCH, VOL. 103, NO. B7, PAGES 15,255–15,268, JULY 10, 1998

Role of faults, nonlinear rheology, and viscosity structure in generating plates from instantaneous mantle flow models

Shijie Zhong[1] and Michael Gurnis

Seismological Laboratory, California Institute of Technology, Pasadena

Louis Moresi

Australian Geodynamics Cooperative Research Centre, CSIRO Exploration and Mining Nedlands, Western Australia, Australia

Abstract. Concentrated strain within plate margins and a significant toroidal component in global plate motion are among the most fundamental features of plate tectonics. A significant proportion of strain in plate margins is accommodated through motion on major tectonic faults. The decoupling influence of faulted plate margins primarily results from history-dependent lithospheric deformation rather than from instantaneous stress-weakening rheologies. For instantaneous mantle flow models, we argue that faults should be treated as preexisting mechanical structures. With models incorporating preexisting faults, a power law rheology with an exponent of 3, and slab pull and ridge push forces, we demonstrate that nonlinear interaction between weak faults and this power law rheology produces plate-like motion. Our models show that in order to produce plate-like motion, the frictional stress on faults needs to be small and the asthenosphere viscosity should be much weaker than that of lithosphere. While both plateness and the ratio of toroidal to poloidal velocities are reduced with increasing fault coupling, the viscosity contrast between the lithosphere and asthenosphere only influences plateness. This shows that both diagnostics, plateness and the ratio of toroidal to poloidal velocities, are necessary to characterize plate motion. The models demonstrate that weak transform faults can guide plate motion. This guiding property of transform faults and the decoupling of thrust faults result in oblique subduction where the strike of subducted slabs is oblique to transform faults. Subducted slabs beneath a dipping fault produce oceanic trench and fore bulge topography and principal stresses consistent with subduction zone observations.

1. Introduction

According to the theory of plate tectonics, plates are nearly rigid with negligible internal strain and with strain concentrated within plate margins [*Wilson*, 1965; *Morgan*, 1968]. Moreover, plate motion is approximately equally partitioned between poloidal (i.e., motion associated with the creation and destruction of plates) and toroidal (i.e., strike-slip motion and plate spin) velocities [*Hager and O'Connell*, 1979]. A significant amount of strain is accommodated in plate margins through earthquakes on major faults between plates [*Davies and Brune*, 1971; *Kanamori*, 1977]. An understanding of the dynamics of plate tectonics is a central goal of geodynamics, not only because plate tectonics is one of the most important features of the Earth but also because plates have a first-order influence on the dynamics of the deep interior [*Hager and O'Connell*, 1979; *Davies*, 1988; *Gable et al.*, 1991].

Two classes of methodologies have been applied to the problem of coupling plates to mantle flow: one based on a force balance and another based on rheology. In the first method, plates with a preset geometry are assumed perfectly rigid; velocity for each plate is determined by balancing torques and forces that act on the plate from mantle flow [*Hager and O'Connell*, 1981; *Ricard and Vigny*, 1989; *Gable et al.*, 1991]. These models are capable of reproducing plate motion by using seismically determined mantle buoyancy structures [*Ricard and Vigny*, 1989] or estimated subducted slab density anomalies based on the history of plate motion [*Lithgow-Bertelloni and Richards*, 1995]. Since plates are derived by definition in these models, they can only address questions of the plate driving mechanism and the influence of plates on the mantle [*Hager and O'Connell*, 1981] rather than answering the question of plate generation. This methodology simplifies the dynamics of plates and margins by using laterally homogeneous viscosity and prescribed boundary velocities for plates. Potentially important plate boundary forces [e.g., *Forsyth and Uyeda*, 1975] are often ignored in torque or force balances [*Ricard and Vigny*, 1989; *Gable et al.*, 1991].

The second methodology does not assume perfectly rigid plates, rather a complex mantle rheology is used in the hope of producing plate-like surface motion from the solution of the momentum equation. Creep experiments on mantle rocks indicate that mantle rheology is both temperature- and stress-dependent. The overall form of effective viscosity can be expressed with

$$\mu_{eff} = A^{1/n} \dot{e}^{1/n-1}, \quad (1)$$

[1]Now at Department of Earth, Atmospheric, and Planetary Sciences, Massachusetts Institute of Technology, Cambridge.

Copyright 1998 by the American Geophysical Union.

Paper number 98JB00605.
0148-0227/98/98JB-00605$09.00

where n is the exponent and is unity for a Newtonian rheology; A is the preexponent which depends on temperature, pressure, and composition; $\dot{e}$ is the second invariant of a strain rate tensor. For mantle rocks, the exponent n is about 3 (i.e., stress weakening) [e.g., *Karato and Wu*, 1993]. Equation (1) is recast from the stress-strain rate relationship (Figure 1). Stresses may be high in plate margins, and this is manifest with existence of a few kilometers of trench topography in converging margins. Earlier two-dimensional (2-D) models with prescribed weak zones, representing plate margins, enforce a localized deformation in weak zones [*Kapitzke*, 1979; *Schmeling and Jacoby*, 1981; *Jacoby and Schmeling*, 1982]. The weak zones in these models were intended to mimick the stress weakening of the lithosphere and mantle inherent in equation (1), although additional weakening processes probably occur in plate margins, such as those dependent on lithology, volatiles [*Lenardic and Kaula*, 1994], and deformation history [*Gurnis*, 1997]. This weak zone formulation has been extensively used in modeling plates in two dimensions [*Gurnis*, 1988; *Gurnis and Hager*, 1988; *Davies*, 1989; *King and Hager*, 1990; *Zhong and Gurnis*, 1994a; *Puster et al.*, 1995].

Considerable effort in modeling plate generation has been directed toward incorporating non-linear stress or stress-weakening rheology into dynamic models [*Christensen*, 1983; *Weinstein and Olson*, 1992; *Bercovici*, 1993, 1995; *Solomatov and Moresi*, 1997]. Models which utilize the power law rheology (equation (1)) with exponents in the range of 3 to 5 predict surface motion which has substantial internal strain but with only a few percent toroidal component [*Christensen*, 1983; *Christensen and Harder*, 1991]. By using thin plate models, *Weinstein and Olson* [1992] and *Bercovici* [1993] have shown that only when a much stronger nonlinear rheology is utilized can a concentrated strain or plate-like surface motion be achieved. The nonlinearity increases with n, but the nonlinearity is strongest when the exponent is -1 as used in models considered by *Bercovici* [1993]. When n=-1, the power law rheology gives two possible branches of strain rate for a given stress, one normal branch with a small strain rate and the other branch with a larger strain rate [*Bercovici*, 1993]. For n as high as 20, the width of regions with concentrated strain (i.e., plate margins) is quite large [*Weinstein and Olson*, 1992], but models with n=-1 produce much narrower margins [*Bercovici*, 1993]. Recently, this n=-1 rheology has been implemented in a three dimensional model [*Tackley*, 1998]. *Solomatov and Moresi* [1997] used a pseudo-plastic rheology (i.e., n is infinite) with depth-dependent yield stress to model the plates, but the emphasis of their models is how a different yield stress can lead to a different style of convection (i.e., stagnant lid or mobile plate). Models with a strong nonlinear rheology apparently have the advantage over models with prescribed weak zones in that plate geometry and surface motion naturally emerge from the dynamics. However, there are significant implications of this methodology. Implicit to the stress weakening rheology is that the weakening processes are instantaneous. Essentially, the models imply that as long as the stress is high, weak fault zones will develop instantaneously, independent of deformation history. This may be inconsistent with observations.

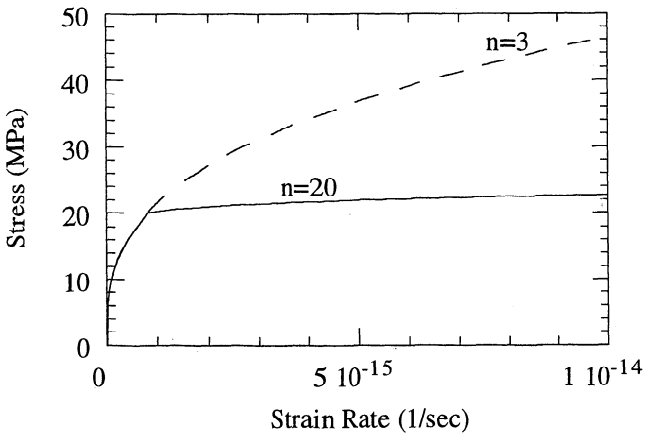

Figure 1. The stress and strain rate relationship for a power law rheology with n=3 and a pseudo-plastic rheology with n=20 for stress larger than 20 MPa. The dimensional preexponent A is 7.9×10^{-8} Pa^{3}s (i.e., nondimensional A is 2×10^7).

According to the studies by *Jeffreys* [1970] and *Artyushkov* [1973], the large topography variation in regions near seamounts and orogenic belts induce large local stresses. With strongly nonlinear stress-weakening rheology (e.g., the pseudo-plasticity or with n=-1), these high stress regions should develop weak fault zones and deform in the same way as plate margins. On the contrary, regions near large intraplate seamounts and old mountain belts do not show noticeable strain. On the other hand, transform fault plate margins, like the San Andreas, do not show high stresses [*Lachenbruch and Sass*, 1988], but significant deformation occurs within the fault zones. A traditional explanation, from *Kanamori* [1980], is that lithospheric strength itself is highly heterogeneous. Here the strength is defined as the deviatoric stress that the lithosphere can support without deforming [*Jeffreys*, 1970]. *Kanamori* [1980] has suggested that heterogeneous strength results from the distribution of weak faults which may be weak due to weak material within faults. Another possible explanation is to invoke the n=-1 rheology whose duality of strain rates can account for the apparently uncorrelated stress to strain rate. Physical mechanisms including void generation and volatile ingestion may lead to the n=-1 rheology [*Bercovici*, 1998]. However, more studies, both theoretical and experimental, are clearly needed in applying this rheology to lithospheric deformation. In summary, we make the following observational inferences: (1) the instantaneous stress weakening is not the primary cause for generating weak fault zones, although it may play a role, even a fundamental role, in lithospheric deformation; and (2) at any instant in time, the existence of weak fault zones reflects the deformation history rather than instantaneous stress.

With the recognition of these fundamental properties of lithospheric strength, it has become clear to us that a simple weak zone formulation, originally from *Kapitzke* [1979], *Schmeling and Jacoby* [1981], and *Jacoby and Schmeling* [1982], has its own merits in capturing the fundamental features of history-dependent lithospheric rheology. Owing to its simplicity, however, the weak zone formulation has considerable drawbacks as a description of plate margin processes. Seismological studies suggest that most lithospheric deformation in converging margins is accommodated through great thrust earthquakes on thrust faults [*Davies and Brune*, 1971; *Kanamori*, 1977; *Ruff and Kanamori*, 1983]. Faults are discontinuities between plates. In the weak

zone formulation, the deformation is distributed over entire weak zones, typically a few hundred kilometers wide. Improving upon these weak zone models, *Zhong and Gurnis* [1994b, 1995, 1996] developed two- and three-dimensional finite element models of a mantle with preexisting faults directly incorporated into a mantle with a power law rheology. In these models, only faults are specified to be weak, although the stress may weaken the media surrounding the faults according to the power law rheology. In these models, faults are simulated as internal lines or planes across which normal velocities are continuous but tangential velocities may be discontinuous. Flow on either side of a fault can be coupled through frictional stress [*Zhong and Gurnis*, 1994b]. Moreover, only fault geometry is prescribed such that the sense of motion on faults (e.g., thrust or strike slip) is determined by the dynamics.

In their 2-D models, *Zhong and Gurnis* [1995] have shown that faulted converging plate margins may contribute to producing plate-like surface motion such that the dynamically determined motion of faulted margins is an essential ingredient to the evolution of plate size and subduction dynamics. 3-D models include both transform and thrust faults and suggest that the interaction between weak faults and a power law rheology is essential to giving rise to plate-like motion [*Zhong and Gurnis*, 1996]. This study is an extension of the report by Zhong and *Gurnis* [1996]. We include high resolution 2-D models with curved fault and pseudo-plastic rheology, and more 3-D models with a variety of vertical and horizontal viscosity structure, all of which were not presented by *Zhong and Gurnis* [1996]. First, we will present numerical techniques for modeling faults in two and three dimensions; second, we will briefly show the influence of a dipping fault on stress and flow fields in a 2-D model of subduction zone; third, we will detail the influence of fault geometry, fault strength, and vertical viscosity structure on plate generation; and finally, we will discuss the implications of our model results to mantle dynamics.

2. Description of Models and Numerical Methods

The governing equations for mantle flow are derived from the conservation of mass and momentum. Since the mantle has a very high Prandlt number, the inertial forces can be ignored in the equation of motion. With the assumption of incompressibility, the momentum and continuity equations are respectively,

$$\sigma_{ij,j} + \rho g \delta_{i2} = 0, \tag{2}$$

$$u_{i,i} = 0, \tag{3}$$

where σ_{ij}, u_i, ρ, and g are the stress tensor, the flow velocity, the density, and gravitational acceleration, respectively. The density may include contributions from temperature variation. The constitutive law is

$$\sigma_{ij} = -P\delta_{ij} + 2\mu_{eff}\dot{e}_{ij}, \tag{4}$$

where

$$\dot{e}_{ij} = (u_{i,j} + u_{jj})/2, \tag{5}$$

P is the pressure, δ_{ij} is the unit tensor, and μ_{eff} is the effective viscosity and is defined in equation (1). It is essential to recognize that (1) whether a model produces plate-like surface motion is entirely determined by the solution of equations (2) and (3) for a given rheology and density structure; (2) while history-dependent rheology may nominally be introduced through the preexponent of A, the rheological equation (1) is only applicable to continua and cannot be used for faults of discontinuous nature. Boundary conditions of the models are free slip on both the bottom and top boundaries and reflecting on side walls.

Although we will concentrate on the influences of preexisting faults and n=3 power law rheology, we will also explore the influences of highly nonlinear stress-weakening rheologies on the generation of plates, particularly the influences of a pseudo-plastic rheology. We choose to use a pseudo-plastic rheology over other stress-weakening rheologies because the pseudo-plastic rheology gives a reasonable numerical convergence rate while containing the basic features of stress-weakening rheologies. For the pseudo-plastic rheology, the exponent n in equation (1) is assumed to be much larger than 3 when stress is larger than a yield stress (Figure 1). We refer to this rheology as "pseudo-plastic" because it differs fundamentally from the normal use of plasticity in rocks [*Jaeger*, 1969]. Normally, plasticity is used to describe the transitional deformation of material from elastic to ductile failure or flow regimes under a sufficiently large stress (i.e., yield stress) and is defined in terms of a stress-strain relationship [*Jaeger*, 1969], not a stress-strain rate relationship. Presumably, deformation in the plastic flow regime after the yield stress is reached can be described as viscous deformation or even linear viscous deformation. Pseudo-plastic rheology is based on a stress-strain rate relationship and implies that fluid viscosity is greatly reduced when stress is larger than a yield stress (Figure 1). In essence, pseudo-plastic rheology is a special form of a nonlinear viscous rheology. Similar pseudo-plastic rheologies have been applied to viscous flow models of the mantle by *Sleep* [1975] and more recently by *Solomatov and Moresi* [1997].

Our 3-D models in a Cartesian domain include a half-space cooling thermal boundary layer and cold subducted slabs (e.g., the geometry of one type of calculation is shown in Figure 2). The buoyancy is derived as if a region, $\Re$, is spreading from the left side boundary at a velocity of 3 cm yr^{-1} (Figure 2). In $\Re$, the surface age increases with distance from the spreading center, and outside of $\Re$, excluding the slabs, the thermal structure is identical to that with the oldest age (Figure 2). A 100 km thick slab extends from a depth of 100 km to 670 km with a 60^0 dip angle (Figure 2). Slab buoyancy is identical to that of the lithosphere just prior to subduction. The viscosity in the upper mantle including the top 100 km layer is determined by a power law rheology with n=3, while the viscosity in the lower mantle is Newtonian and equal to 2×10^{22} Pa s. Temperature dependence of viscosity is simulated with the power law preexponent A such that a larger A is used for both slabs and the upper 100 km. At the spreading center, a narrow region within the top 100 km layer has a smaller A to account for the higher temperature and partial melting below a ridge. For most calculations undertaken, A for the top 100 km layer and slabs, the spreading centers, and the upper mantle are 2×10^7, 2×10^3, and 20, respectively. These preexponents are chosen such that the average effective viscosities for the top 100 km and the upper mantle are about 10^{23} Pa s and 2×10^{20} Pa s, respectively, and that the average surface velocity in $\Re$ is close to the velocity used to derive the input buoyancy fields.

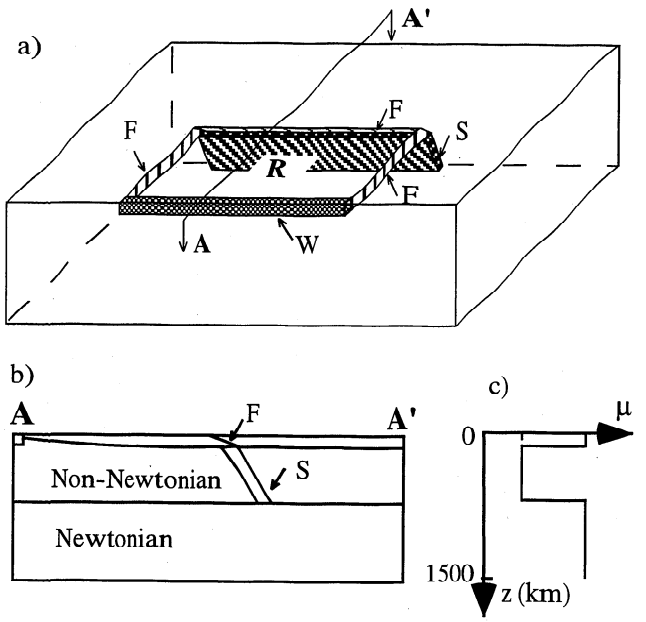

Figure 2. (a) The geometry of the three-dimensional flow model with faults, (b) a cross-section AA' of the model for viscosity and thermal structure, and (c) the average viscosity profile. In Figure 2a, F, S, and W stand for faults, slab, and weak zone, respectively. In Figure 2c, viscosity is normalized by 2×10^{22} Pa s. The density, thermal diffusivity, and thermal expansivity for the mantle are 3300 kg m^{-3}, 10^{-6} m s^{-2}, and $2\times10^{-5}K^{-1}$, respectively.

$\Re$ is bounded by faults with different dips which dissect the upper 100 km (high viscosity) layer, except for the side with the spreading center (Figure 2). Fault dip is 30^{o} when the fault is above a slab but vertical elsewhere. In the 2-D models, fault dip may steepen with the depth. In converging margins, seismically active faults do extend to greater than 60 km depth [*Tichelaar and Ruff*, 1993], but the faults (at least for the seismogenic portion) are shallower in transform fault plate boundaries. Because the top 100 km layer is assumed to have a uniformly high preexponent A, for simplicity, we assume a uniform 100 km fault depth in our models. Transform faults that offset spreading centers are usually shorter but occur with a large frequency, compared to vertical faults in the model (Figure 2). In the model, the short transform faults are represented by a single long transform fault. Moreover, our long transform fault model also partly results from projection onto a Cartesian domain. For example, the northern and southern boundaries of the Pacific plate have a small length because of their proximity to the Pacific plate's pole of rotation.

The influence of faults on stress and deformation fields has been previously studied in other geophysical contexts numerically [e.g., *Melosh and Williams*, 1989; *Barr and Houseman*, 1992, 1996; *Bird and Kong*, 1994]. We use constrained elements and matrix transformation techniques to simulate faults of arbitrary geometry. These techniques are generalized from *Zhong and Gurnis* [1994b] (see Appendix A). Faults are simulated as internal interfaces across which normal velocities are constrained to be continuous, but tangential velocities may be discontinuous. We emphasize that only fault geometry is prescribed while the sense of motion on faults (e.g., thrust or strike slip) is determined by the dynamics. Although for most calculations, the frictional stress on faults is zero, we explore nonzero frictional stress with prescribed values on faults.

We use a finite element method to solve equations (2) and (3) with nonlinear rheology and faults. The finite element software, Citcom, used in this study is based on a primitive variable formulation with two-level iterations to solve the pressure and velocity simultaneously [*Moresi and Solomatov*, 1995; *Moresi and Gurnis*, 1996]. Both multigrid and preconditioned conjugate gradient solvers are included in the inner level iteration in Citcom, while only a preconditioned conjugate gradient solver is used in this study because of the complex 3-D meshes resulting from the inclusion of faults. We have ported the software to massively parallel computers (see Appendix B). With the use of parallel computers, we are able to solve models with significantly higher resolution than presented by *Zhong and Gurnis* [1996]. For most 3-D calculations, we use about 1.5×10^{5} linear elements (i.e., 8 nodes per element). The finite element mesh was refined near the faults, slabs, and top 100 km with horizontal and vertical spacing of about 15 km. The nonlinear momentum equation is solved iteratively until relative variation in velocity between two consecutive iterations is less than 1%.

To characterize plate-like surface motion, we define the ratio of toroidal to poloidal components $R_{T/P}$ [*Gable et al.*, 1991] and plateness P as

$$R_{T/P}=\sqrt{\sum_{l,m}\frac{(k_y V_x^{lm}-k_x V_y^{lm})^2}{k_x^2+k_y^2}\Big/\sum_{l,m}\frac{(k_x V_x^{lm}+k_y V_y^{lm})^2}{k_x^2+k_y^2}}, \quad (6)$$

$$P=1-V_{rms}/V_p, \quad (7)$$

$$V_p=\sqrt{\bar{u}_x^2+\bar{u}_y^2}, \quad (8)$$

$$\bar{u}_x=\frac{1}{\Re}\int_{\Re}u_x ds, \qquad \bar{u}_y=\frac{1}{\Re}\int_{\Re}u_y ds, \quad (9)$$

where $k_x=2\pi/L_x$ and $k_y=2\pi/L_y$ are the wavenumbers in x and y directions; L_x and L_y are the horizontal dimensions of the box in x and y directions; integer indices l and m cannot be both equal to zero; V_x^{lm} and V_y^{lm} are the spectra of surface velocity of x and y components associated with l and m; V_p is the magnitude of average velocity $(\bar{u}_x,\bar{u}_y)$ in region $\Re$; and V_{rms} is the RMS deviation from $(\bar{u}_x,\bar{u}_y)$ in $\Re$ (Fig. 2). Plateness defined here is different from that used in 2-D studies by *Weinstein and Olson* [1992]. Plateness is 1 for a perfectly rigid plate and is 0.52 for a sinusoidal variation in surface velocity along the spreading direction in $\Re$. Since $R_{T/P}$ is geometry-dependent [*Olson and Bercovici*, 1991], we define a normalized ratio of toroidal to poloidal components, $N_{T/P}$, which is $R_{T/P}$ normalized by the ratio of toroidal to poloidal components for a perfectly rigid plate within region $\Re$.

3. Results

In this section, we will first show the influence of a dipping fault positioned directly above a subducted slab on plate velocity, stress, and strain rate. Then, we will focus on 3-D problems with multiple faults. For 3-D models, we will examine the roles played by viscosity structure, fault strength,

and fault geometry on plate generation. We will end with a discussion on the implications of our results to the Earth.

3.1. Two-Dimensional Models

Previously, the role which a dipping fault has on the dynamic support of outer rise, trench, and back arc topography in subduction zones has been investigated with 2-D viscous [*Zhong and Gurnis*, 1994b] and viscoelastic models [*Gurnis et al.*, 1996]. Here, we build upon this earlier work and examine the influence of a dipping fault on stress, strain rate, and flow fields within lithosphere and mantle. The 2-D models should be viewed as cross sections dissecting the 3-D models of a subducted slab and spreading center described next (e.g., the cross section AA' in Figure 2). The rheological parameters and buoyancy structure are the same as those in 3-D models. Therefore the 2-D models can be directly compared with the 3-D models. With our higher- resolution 2-D models, we are able to directly explore the influence of fault geometry, especially the influence of a curved dipping fault with a smaller dip at a shallower depth. This latter model with a curved dipping fault is more realistic than our earlier models with a straight fault and allows better comparisons of stress and strain rate with seismic observations. A mesh with 192x64 bilinear elements is used and is refined near the subducted slab and within the top 100 km layer.

3.1.1. Models with and without a dipping fault. With no fault (case 1 in Table 1), the mantle flow induced by the slab and oceanic plate shows that (1) the horizontal velocity of the subducting plate is about 1.3 cm yr^{-1}, significantly greater than that of the overriding plate (Figures 3a and 4a); (2) a significant portion (~500 km in width) of the overriding plate is actively deforming and moving with a substantial horizontal velocity toward the overriding plate (Figures 3a, 3d and 4a); (3) although concentrated in the upper mantle, flow extends into the high viscosity lower mantle beneath the overriding plate (Figure 3a). In comparison with the upper mantle, the effective viscosities for the lithosphere and subducted slab are higher (Figure 3a). The averaged viscosities for the oceanic plate, $slab_{24}$ and upper mantle below the subducting plate are about $2x10^{22}$ Pa s, $4x10^{22}$ Pa s, and $4x10^{20}$ Pa s, respectively. In the top 100 km layer, besides a weak spreading center derived from a reduced exponent A, a weak zone develops above the slab with a viscosity of about $2x10^{22}$ Pa s (Figures 3a and 3d).

The strain rate is concentrated near the material boundaries (e.g., regions surrounding the slab and beneath the lithosphere) and in the weak zones in the top 100 km layer (Figures 3b and 3e). In the top 100 km layer excluding the weak spreading center, the largest strain rate (~$2x10^{-15}$ s^{-1}) occurs directly above the slab (Figure 3e). The deviatoric stress in the lithosphere, slab, and lower mantle near the slab is much larger compared to other regions and is largest within and above the slab (Figure 3c). The principal stresses show a horizontal compression in the overriding plate and a

Table 1. Model Parameters

Case	Model Description				V_p, cm/yr	P	$N_{T/P}(R_{T/P})$	μ_{lith}/μ_{um}
	Geometry	Rheology	Faults	F, MPa				
1	2D1	M1	N	--	1.3	0.96	--	$5.5x10^3$
2	2D1	M1	Y	0	2.8	0.96	--	$3.7x10^3$
3	2D1	M1	Y	0	2.3	0.96	--	$4.1x10^3$
4	2D1	M1P	N	--	2.8	0.96	--	$3.3x10^3$
5	2D1	M1P	N	--	5.0	0.96	--	$2.1x10^3$
6	3D1	M1	N	--	0.98	0.74	0.49(0.27)	$2.3x10^2$
7	3D1	M1	Y	0	3.3	0.91	0.87(0.48)	$3.1x10^2$
8	3D1	M2	Y	0	0.16	0.49	0.16(0.09)	$3.1x10^2$
9	3D1	M3	Y	0	0.44	0.82	0.36(0.20)	$2.2x10^2$
10	3D1	M4	Y	0	2.3	0.89	0.89(0.49)	$2.8x10^2$
11	3D1	M1	Y	5	2.6	0.87	0.80(0.44)	$2.7x10^2$
12	3D1	M1	Y	10	2.1	0.82	0.73(0.40)	$2.3x10^2$
13	3D1	M1	Y	20	1.4	0.72	0.56(0.31)	$2.0x10^2$
14	3D1	M5	Y	0	2.2	0.83	0.87(0.48)	$1.4x10^2$
15	3D1	M6	Y	0	1.1	0.62	0.80(0.44)	50.2
16	3D1	M7	Y	0	0.96	0.94	0.89(0.49)	$6.1x10^2$
17	3D2	M1	N	--	0.91	0.74	0.51(0.28)	$2.7x10^2$
18	3D2	M1	Y	0	2.9	0.89	0.87(0.48)	$3.0x10^2$
19	3D3	M1	N	--	0.97	0.72	0.65(0.41)	$2.7x10^2$
20	3D3	M1	Y	0	2.9	0.88	0.90(0.57)	$3.5x10^2$

2D1 and 2D2 are for slab dips 60^o and 30^o, respectively; 3D1, 3D2, and 3D3 are for three different geometries that are shown in Figure 6 and 11. M1-M7 represent different rheology models: M1, A=($2x10^7$, $2x10^7$, $2x10^3$, $2x10^1$) and n=(3, 3, 3, 3); M2, A=(5.6, $1.8x10^{-2}$, 5.6, $1.8x10^{-2}$) and n=(1, 1, 1, 1); M3, A=(5.6, $5.0x10^{-1}$, $9x10^{-3}$, $1.8x10^{-2}$) and n=(1, 1, 1, 1); M4, A=($2x10^7$, $5x10^{-1}$, $9x10^{-3}$, $1.8x10^{-2}$) and n=(3, 1, 1, 1);M5, A=($2x10^7$, $2x10^7$, $2x10^3$, $2x10^2$) and n=(3, 3, 3, 3); M6, A=($2x10^7$, $2x10^7$, $2x10^3$, $2x10^3$) and n=(3, 3, 3, 3); M7, A=($2x10^8$, $2x10^8$, $2x10^3$, $2x10^1$) and n=(3, 3, 3, 3), where the numbers in parentheses are the preexponents and exponents for the top 100 km layer, slab, spreading center, and upper mantle. M1P is for M1 rheology model with pseudo-plastic rheology for the top 100 km layer. F gives the frictional stress on faults. $R_{T/P}$ for a perfectly rigid plate with geometry 3D1, 3D2, and 3D3 are 0.55, 0.55, and 0.63, respectively.

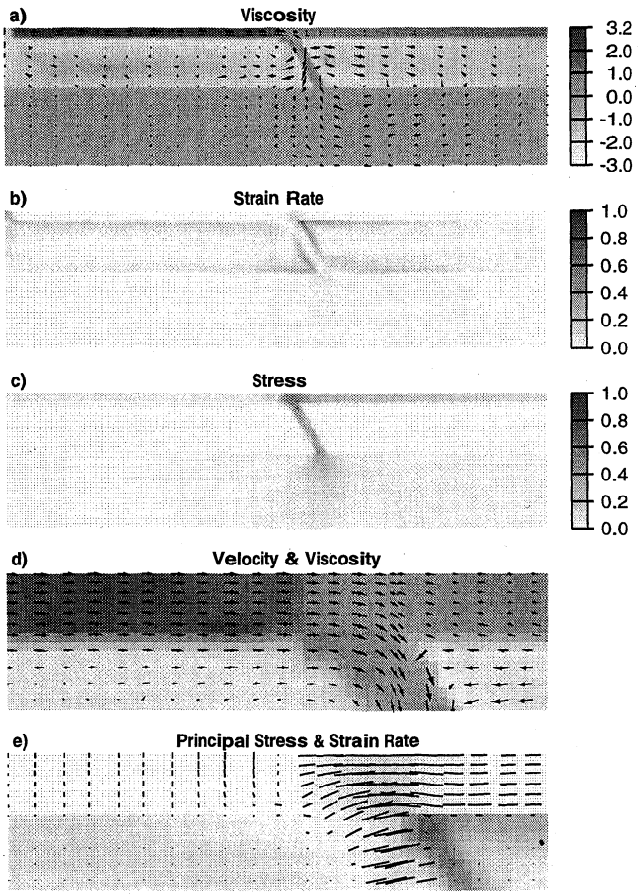

Figure 3. (a) Effective viscosity and flow velocity (vectors), (b) second invariants of strain rate and (c) stress for 2D case without a fault (case 1). Magnified views in the vicinity of slab show (d) effective viscosity and flow velocity and (e) second invariant of strain rate and principal compressive stress. In Figure 3e, the length and orientation of each line represent the magnitude and direction of principal compressive stress. The viscosity, stress, and strain rate are normalized by 2.0×10^{22} Pa s, 71.1 MPa, and 1.78×10^{-14} s^{-1}. The effective viscosity is in a logarithmic scale.

horizontal extension in the subducting plate (Figure 3e). Within the slab, the stress is downdip extensional at the shallow part (Figure 3e), and turns into downdip compressional at a depth of about 500 km, similar to the finite element models by *Vassiliou and Hager* [1988]. Topography decreases with distance from the spreading center as expected for a cooling plate but becomes a significant depression (about 500 km in width and 2.4 km in amplitude) directly above the slab (Figures 4c and 4d). The maximum depression in dynamic topography occurs approximately in the location of maximum strain rate (Figures 4c, 4d, and 4e).

We now investigate the influence of a dipping fault on stress, strain rate, and flow fields in subduction zones. A curved dipping fault is included in case 2 which is otherwise identical to the preceding case (Table 1). The horizontal distance between the two end points of the fault is 200 km (Figure 5), consistent with what has been inferred for most subduction zones [e.g., *Jarrard*, 1986]. The fault dip steepens with depth and is about 25° when it intersects the surface (Figure 5). Compared with the case with no fault (case 1), the inclusion of the dipping fault does not change the overall patterns of viscosity (Figure 5a), strain rate (Figure 5b), and stress (Figure 5c). However, we observe significant changes in the velocity (Figures 4a, 5a, and 5d), stress and strain rate within the top 100 km layer (Figures 5c, 5d, and 5e). The subducting plate velocity is now about 2.8 cm yr^{-1}, more than twice the rate of the preceding case with no fault (case 1). The velocity above the slab is now substantially larger in the subducting plate compared to the overriding plate. The subducting plate velocity along the fault is nearly parallel to the tangent of the dipping fault (Figure 5d). Across the fault, the tangential velocity is discontinuous and the relative motion is comparable with convergence velocity between subducting and overriding plates (Figures 4a and 5d). This discontinuous tangential velocity arises from fault decoupling and differs from the preceding case with no fault (case 1) in which velocity everywhere is continuous (Figure 3d).

While horizontal compression persists in the overriding plate, the magnitude of the compressional stress is reduced

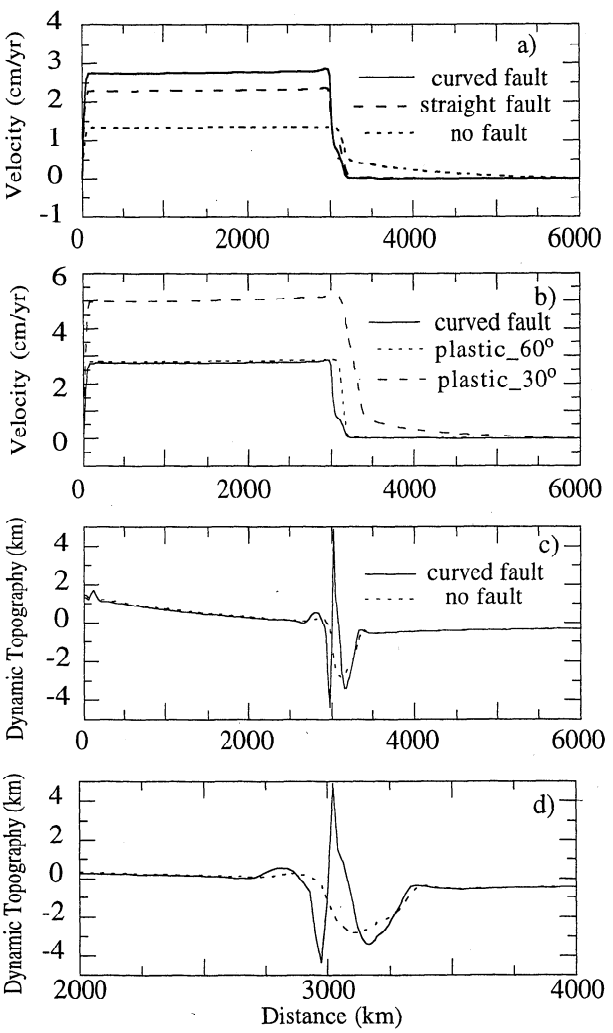

Figure 4. Surface velocity profiles (a) for the 2-D cases with no fault (case 1) and with curved and stright faults (cases 2 and 3) (a) and (b) for the cases with the pseudo-plastic rheology and different slab dip (cases 4 and 5), (c) dynamic topography, and (d) magnified view of dynamic topography for the cases with no fault (case 1) and with a curved fault (case 2). Also plotted in Figure 4b is the surface velocity for case 2 with a curved fault.

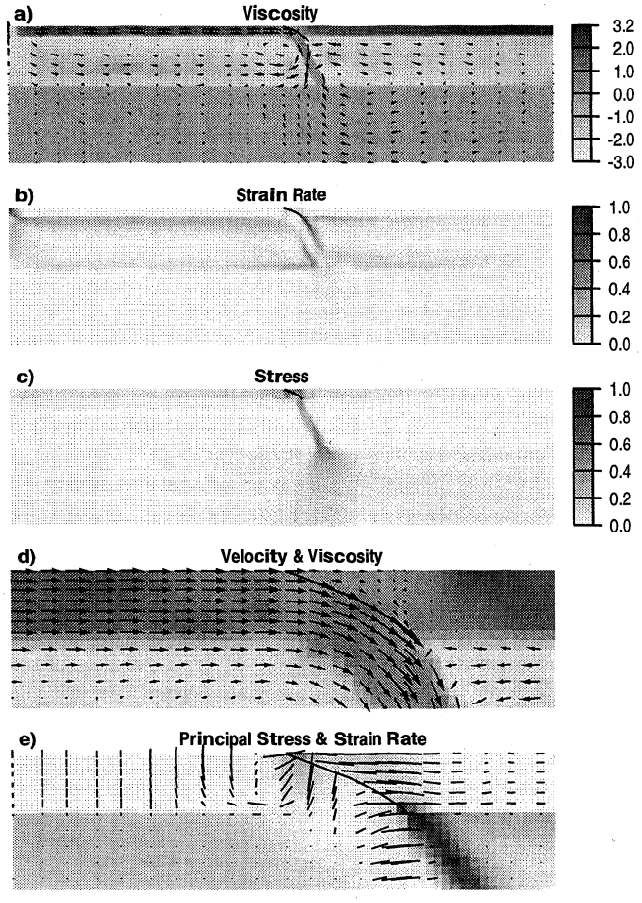

Figure 5. (a) Effective viscosity and flow velocity (vectors), (b) second invariants of strain rate and (c) stress, and (d) magnified views of effective viscosity and flow velocity and (e) second invariant of strain rate and principal compressive stress for case 2 with a fault. See Figure 3 for more details.

(Figure 5e), compared with the case without a fault (Figure 5e). But more significantly, within the subducting plate directly beneath the fault, principal compressional stress is rotated so that it is approximately perpendicular to the fault, indicating a downdip extension (Figure 5e). As we will discuss later, this downdip extension in the top 100 km layer is remarkably similar to seismic observations, but this is not a prediction from the case without a fault (Figure 3e for case 1). There is also significant strain rate beneath the fault (~2×10^{-15} s^{-1}) (Figure 5e). On the oceanic plate and near the fault, the topography is characterized by an outer rise (~0.4 km in amplitude and 200 km in width) and trench (~4 km in amplitude and 100 km in width). On the overriding plate, topography is elevated near the fault and is low over the subducted slab (Figures 4c and 4d). We also compute a case (case 3) which is identical to case 2 except that the fault is straight. The overall features including stress and strain rate, and topography from this straight fault calculation are similar to those from the curved fault case (case 2), but the surface velocity is reduced by about 20% to 2.3 cm yr^{-1} (Figure 4a). This case shows that models with a straight fault [e.g., *Zhong and Gurnis*, 1994b] capture all the important features for faults with variable dip angles. Therefore, for dipping faults in our 3-D models, we will assume that the dip angles do not vary with depth.

3.1.2. Models with a pseudo-plastic rheology. Given the important influence of a dipping fault, it is interesting to examine whether a highly nonlinear stress-weakening rheology alone can reproduce the stress, strain, and flow velocity that are seen in the case with a fault (case 2). We will use two models without faults (cases 4 and 5) and with a pseudo-plastic rheology for the lithosphere to demonstrate that the stress-dependent rheology alone may not reproduce the feature resulting from faults. In the pseudo-plastic rheology used here, the exponent n is assumed to be 20 when the deviatoric stress is larger than a yield stress, 20 MPa, while n is 3 for smaller stresses (Figure 1).

Case 4 is identical to the case without a fault (case 1) except that the pseudo-plastic rheology is used for the lithosphere. Compared with a purely n=3 rheology (case 1), the pseudo-plastic rheology leads to a decrease in both effective viscosity and deviatoric stress but an increase in strain rate in the region above the slab (Figures 6a and 6b for case 4 and Figures 3d and 3e for case 1). This is because the maximum deviatoric stresses in the lithosphere are limited to be around 20 MPa by the pseudo-plastic rheology, which effectively weakens the region above the slab where the stress would be significantly greater than 20 MPa if there was no pseudo-plastic rheology (e.g., case 1). The pseudo-plasticity does not seem to influence the pattern of stress, although the strain rate is more localized and surface velocity is increased (Figures 6b and 4b), compared with case 1 (Figures 3e and 4b).

Compared with the case with a fault and purely n=3 rheology (case 2), the magnitude of surface velocity for the case with pseudo-plasticity (case 4) is approximately the same (Figure 4b), but the stress and strain rate above the slab are

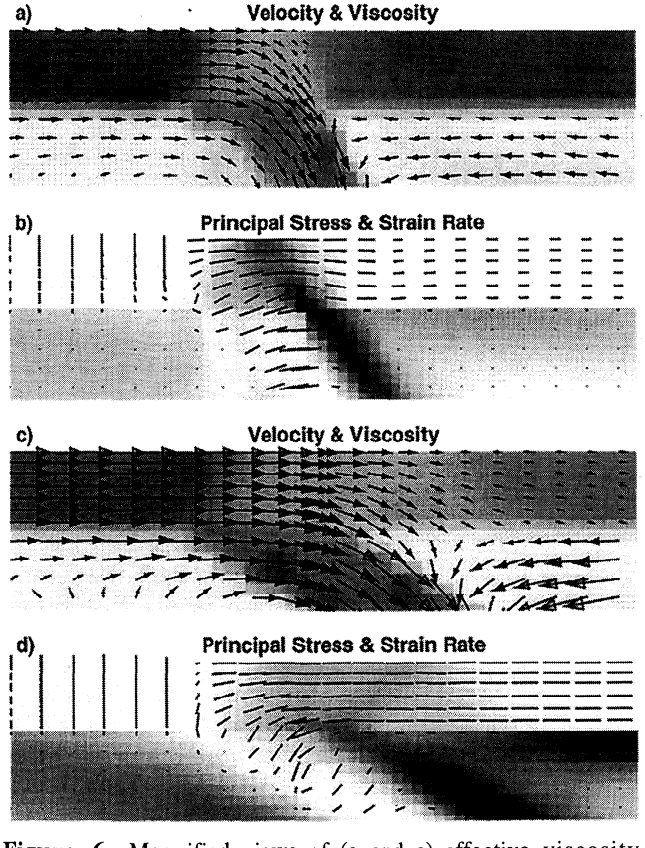

Figure 6. Magnified views of (a and c) effective viscosity and flow velocity and (b and d) second invariant of strain rate and principal compressive stress for cases 4 and 5 with pseudo-plastic rheology, respectively. See Figure 3 for more details.

different (Figures 6a, 6b, 5d, and 5e); the location of the "plate margin" where the horizontal velocity decreases rapidly is about 100 km closer to the overriding plate (i.e., converging velocity has a steep dip angle) (Figures 4b, 6a, and 5d). For this pseudo-plastic case without a fault (case 4), the location of "margin" as well as the stress and strain rate fields are controlled by the buoyancy of the slab. The location of the effective "margin" moves even further toward the overriding plate when slab dip is reduced from 60^{o} in case 4 to 30^{o} in another model (case 5) which is otherwise identical to the preceding case with pseudo-plasticity (case 4) (Figures 4b, 6c and 6d). This is because the maximum of the slab-induced deviatoric stresses moves further into the overriding plate with smaller slab dips (case 5). Both cases with the pseudo-plasticity (cases 4 and 5) show similar stress and strain rate fields (Figures 6b and 6d), although the flow velocity is greater for case 5 with a smaller dip, primarily because of the longer slab and larger buoyancy (the slabs are assumed to reach the same depth, i.e., 670 km).

The flow velocity, velocity jump across the fault, and stress and strain rate beneath the fault (case 2) reflect influence of faults (Figure 5). It seems difficult for models with only pseudo-plastic or stress-weakening rheology with exponent $n>1$ (i.e., cases 4 and 5 and other cases with different yield stresses and exponents) to simulate realistically these features, although the pseudo-plastic rheology can produce weak margins to mobilize surface plates (Figures 4b and 6).

3.2. Three Dimensional Models

While 2-D models are a powerful tool to explore the role of dipping faults, they cannot be used to understand the role of transform faults on plate motion, especially the generation of toroidal motion which is inherently three dimensional. In the following models, we will study the influence of faults in three dimensions.

3.2.1. Models with and without faults. For comparison, our first model (case 6) is the 3-D equivalent of case 1 containing no faults and with slab strike parallel to the spreading center (Figure 7a). The length (i.e., in the spreading direction) and width of the region $\Re$ are 3000 km and 2250 km, respectively. Surface velocities in region $\Re$ vary gradually in both the spreading parallel and perpendicular directions (Figures 7b, 8a, and 8b), indicating a large internal strain rate. The average velocity in region $\Re$, V_p, is about 0.98 cm yr^{-1} and is perpendicular to the spreading center (Figure 7b). Although there is a sudden jump in thermal structure from $\Re$ to the surrounding region along the ridge direction, surface flow is predominantly ridge-perpendicular (Figure 7b). The lack in ridge-parallel surface flow results from the following reasons. The main driving force in this case is the slab, and the bouyancy associated with the jump in thermal structure is secondary because of its short-wavelength and shallow depth. The slab which is parallel to the ridge always tends to excite flow perpendicular to its strike. This effect is further enhanced by the lateral variations in viscosity associated with the slab and ridge which are served as a stress guide. The ratio of toroidal to poloidal components of the surface velocity, $R_{T/P}$, is 0.27, compared to 0.55 for a perfectly rigid plate with this configuration (i.e., $N_{T/P}$=0.49), and plateness P is 0.74 (Table 1). The effective viscosity of both the diverging and converging "margins" are reduced. The effective viscosity in other surface regions varies gradually and reflects the variations in strain rate (Figure 7b). The average viscosity in $\Re$ and in the upper mantle beneath $\Re$ are about 10^{23} Pa s and 5×10^{20} Pa s, respectively. Topography in the region $\Re$ increases with age and distance from the spreading center, as expected, but over the slab there is a broad depression (~500 km in width) (Figure 7c), similar to that from the 2-D calculation (Figures 4c and 4d for case 1).

We now contrast this model (case 6) with a model (case 7) that includes faults with zero frictional stress but is otherwise identical to case 6. The strike of the dipping fault is parallel to the spreading center but perpendicular to the strike of vertical faults (Figure 7d), and the dip angle is constant. We find that surface velocity in region $\Re$ bounded by faults are nearly constant (Figures 7e, 8a and 8b) and parallel to the strike of vertical faults. There are sharp velocity contrasts across the faults (Figures 8a and 8b). V_p is about 3.3 cm yr^{-1}, close to the velocity with which the buoyancy was derived. $R_{T/P}$ and P are 0.48 ($N_{T/P}$=0.87) and 0.91, respectively (Table 1). The gross topography and viscosity are similar to those from the case with no faults (case 6) (Figures 7b, 7c, 7e, and 7f). Like the 2-D model, there is a prominent outer rise (~200 km in width and 0.5 km in amplitude) and a distinct trench (~100 km wide and 4 km deep) near the dipping fault (Figure 7f). In comparison to the fluid near the converging margin, the transform faults are relatively strong (Figure 7f). The average viscosity in $\Re$ and in the upper mantle beneath $\Re$ are about 10^{23} Pa s and 3.6×10^{20} Pa s, respectively. Compared with case 6 without faults, the case with faults (case 7) has a larger

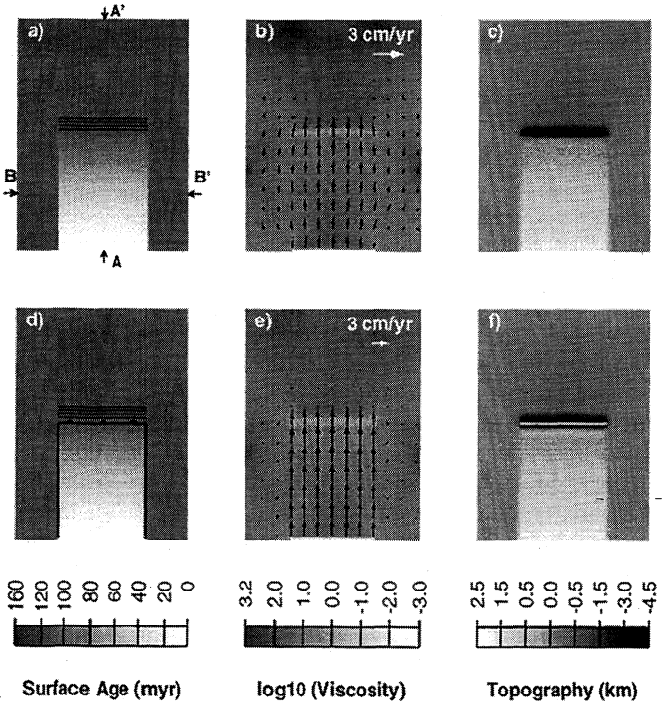

Figure 7. Map view of input buoyancy structure, outputs of surface velocity and effective viscosity, and dynamic topography, for the 3-D cases (a, b, and c) with no fault and (d, e, and f) with faults (cases 6 and 7), respectively. In Figures 7a and 7d, the lines outside $\Re$ show the depth of slabs. In Figure 7d, the lines bounding $\Re$ represent faults; triangles on fault lines indicate a dipping fault. The length, width, and thickness of the model boxes are 6000 km, 4500 km, and 1500 km, respectively.

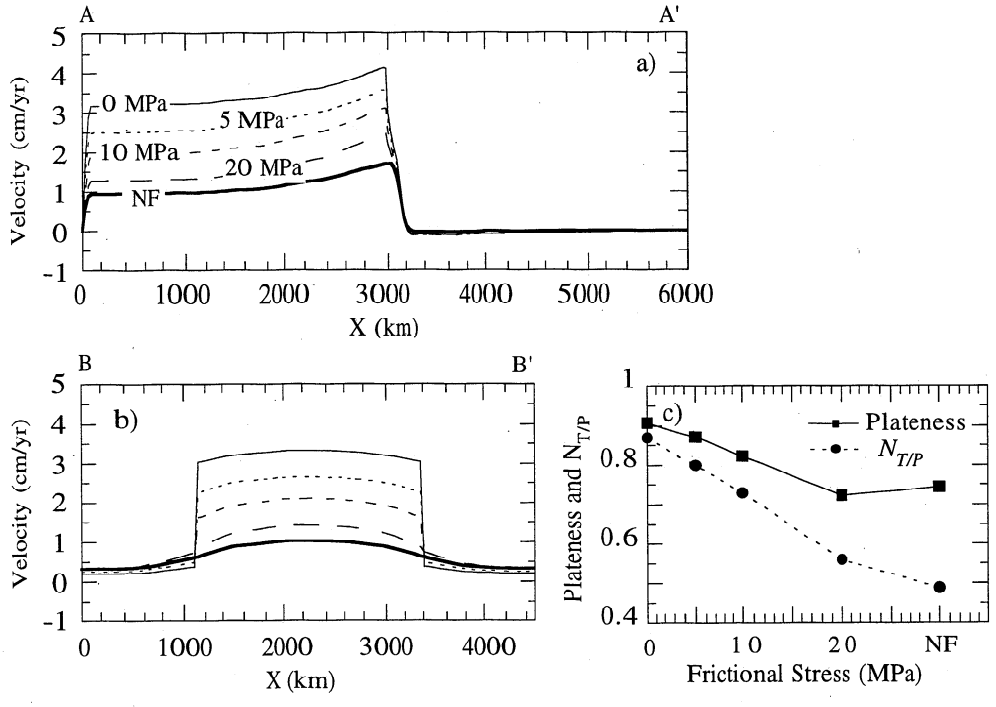

Figure 8. Surface velocities for cross sections (a) AA' and (b) BB', and (c) normalized ratio of toroidal to poloidal components, $N_{T/P}$, and plateness, P for cases without faults (NF for case 6) and with faults of different frictional stress (cases 7, 11, 12, and 13).

viscosity in $\Re$ and this is due to a smaller strain rate in the subducting plate, although the plate has a larger velocity (Figures 7b and 7e), and the larger plate velocity for case 7 causes a greater shearing in the upper mantle and therefore a weaker upper mantle beneath the plate.

3.2.2. Influence of viscosity structure and fault strength. The plate-like surface velocity from case 7 (Figure 7e) (we will refer case 7 as the standard case hereafter) results from a non-linear interaction between weak faults and the stress weakening rheology and weak coupling between plate and asthenosphere. In this section, we will use a series of models with different frictional fault forces and different viscosity structures to demonstrate that weak faults, stress weakening rheology, and weak coupling between plate and asthenosphere are all necessary in order to achieve the plate-like surface motion.

We first show that stress weakening rheology plays an the essential role in generating plate-like motion. Case 8 uses a layered Newtonian viscosity structure (i.e., n=1) without lateral variations in viscosity, but it includes the same buoyancy force and faults as in our standard case (i.e., case 7). The viscosities for the top 100 km layer, the upper mantle (i.e., 100 km to 670 km depth), and the lower mantle are the same as the average effective viscosities for each corresponding layer in the standard case (Table 1). For this case with Newtonian viscosity, surface velocities are greatly reduced in amplitude, and internal strain rate increases such that both plateness and $N_{T/P}$ are greatly reduced (P=0.49 and $N_{T/P}$=0.16) (Figure 9a and Table 1). This indicates that faults alone do not result in the plate-like surface velocity. Augmenting this case with some lateral variations in viscosity, we further include a weak spreading center and strong slab in another Newtonian calculation (case 9 and Table 1). For consistency, the spreading center and slab viscosities are the same as the average effective viscosities for each corresponding regions in the standard case. Compared with the standard case, this Newtonian case with some lateral variations in viscosity (case 9), yields a similar plateness but significantly less toroidal component (P=0.82 and $N_{T/P}$=0.36 in Table 1) (Figure 9b for surface velocity). Based on the preceding case (i.e., case 9), we now change the rheology for the top 100 km layer into the stress weakening rheology used in the standard case, but with other regions remaining Newtonian (case 10 in Table 1). Surface velocities with stress weakening rheology only in the lithosphere (case 10) show similar plate-like features as those in the standard case, with a plateness of 0.89 and $N_{T/P}$ of 0.89 (Figure 9c), indicating that the stress weakening rheology for lithosphere is the essential component for producing plate-like features.

We now demonstrate the importance of weak faults. The standard case with faults (case 7) and our original 3-D model

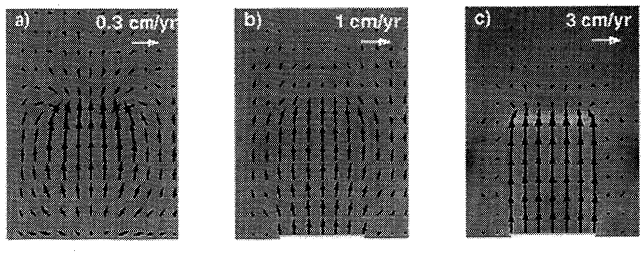

Figure 9. Map views of surface velocity and effective viscosity for (a) the Newtonian case with no lateral variation in viscosity (case 8), (b) the Newtonian case with strong slab and weak spreading center (case 9), and (c) the stress weakening lithosphere (case 10). In all cases, there are weak faults with a geometry shown in Figure 7d.

without faults (case 6) represent two extremes. With no frictional force across the faults, flow is fully decoupled; at the other extreme, where no faults are included, flow is fully coupled. Calculations have been done for cases (cases 11, 12, and 13 in Table 1) with the same fault and buoyancy distribution as for the standard case but with different frictional forces on faults. As the frictional force increases from 0 to 20 MPa, the surface velocity, $N_{T/P}$ and P decrease and progressively resemble those from the case with no faults (Figure 8). These calculations indicate that plateness and toroidal velocity component are sensitive to the frictional force on faults and that plate-like surface motion only arises when there is a low frictional force on faults.

Finally, we show the influence of coupling between lithosphere and asthenosphere on surface motion. We compare our standard case (case 7) with those cases (cases 14, 15, and 16) with different pre-exponents A for the top 100 km layer and the upper mantle to determine the influence of viscosity contrast between plate and the upper mantle (Table 1). These three cases are identical to the standard case (case 7) except for the pre-exponents A. In cases 14 and 15, the pre-exponents are increased only for the upper mantle and remain the same elsewhere, as in the standard case. For these two cases, the increased pre-exponents for the upper mantle increase the upper mantle viscosity and reduce the viscosity contrast (i.e., increase the coupling) between plate and upper mantle, compared with the standard case (Figure 10a and Table 1). The increased coupling between plate and upper mantle reduces the surface velocity in $\Re$ and plateness (Figures 10b and 10c). In case 16, while pre-exponent for the upper mantle is the same as in the standard case, pre-exponents for the top 100 km and slab are increased. Therefore, both the viscosity within plate and the viscosity contrast between plate and the upper mantle are increased (Figure 10a and Table 1). The surface velocity from this case is reduced and shows less variation in $\Re$ (i.e., a larger plateness), compared with the standard case (Figures 10b and 10c), and this is due to the increased lithospheric viscosity. These three cases (cases 14, 15, and 16) along with the standard case (case 7) show that in order to achieve a large plateness the viscosity contrast between lithosphere and the upper mantle should be large (Figure 10d). However, $N_{T/P}$ does not vary significantly with the viscosity contrast (Figure 10d).

3.2.3. Influence of fault geometry. Plates usually have much more complicated geometry in comparison to our standard case. For the Pacific plate, while the strikes of Izu-Bonin and Japanese subduction zones are approximately perpendicular to plate motion, the strike of Aluentian subduction zone is nearly parallel to plate motion. In the case of the Aluentian subduction zone, oblique subduction occurs. We will now demonstrate that fault decoupling is essential for oblique subduction.

We first show a calculation including a slab with a strike oblique to the spreading center (Figure 11a) but no faults (Case 17 in Table 1). While one side of region $\Re$ is 3562 km long, the other side is 1125 km shorter (Figure 11a). The width of region $\Re$ is 2250 km. For this case with no faults, velocities in $\Re$ vary gradually in both magnitude and direction, and velocity becomes nearly perpendicular to the strike of slab near the slab (Figure 11b). Plateness is 0.74 and $N_{T/P}$ =0.51 ($R_{T/P}$ =0.28; $R_{T/P}$=0.55 for a perfect plate of this geometry). The average velocity in $\Re$ is 0.91 cm yr^{-1}. When faults are included in a model (case 18) (Figure 11a) which is otherwise identical to the preceding case (case 17), surface velocities in $\Re$ are nearly parallel to the vertical faults and are approximately uniform (Fig. 11c), showing plate-like

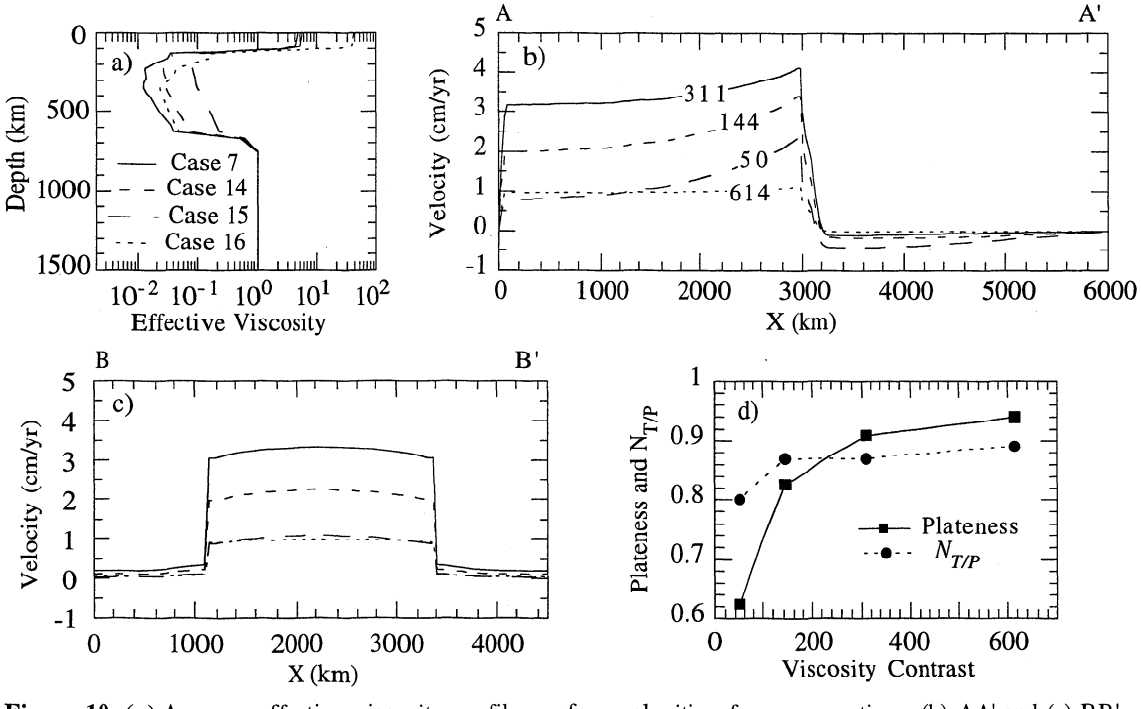

Figure 10. (a) Average effective viscosity profile, surface velocities for cross sections (b) AA' and (c) BB', and (d) normalized ratio of toroidal to poloidal components, $N_{T/P}$, and plateness, P for cases with different viscosity contrast between the lithosphere and upper mantle. The viscosity contrast for each case is marked on velocity profile in Figure 10b.

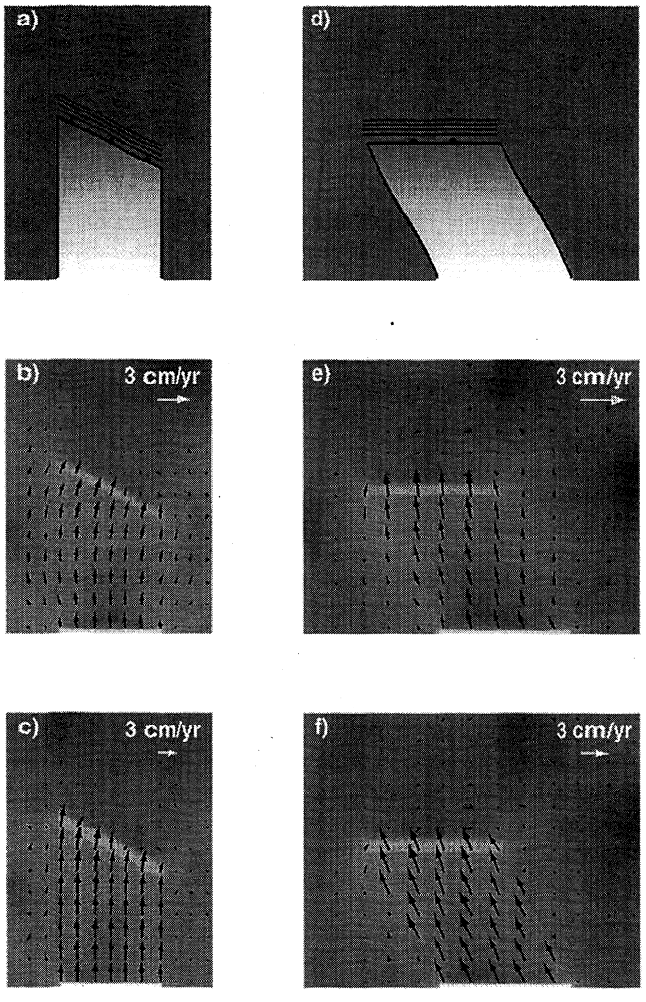

Figure 11. Map views of (a) input buoyancy structure and faults and model outputs of surface velocity and effective viscosity for cases (b) 17 and (c) 18; map views of (d) the buoyancy structure and faults and model outputs of surface velocity and effective viscosity for cases (e) 19 and (f) 20. For cases 19 and 20, the length, width, and thickness of the model boxes are 6000 km, 7500 km, and 1500 km, respectively.

behavior with P=0.89 and N_T / P=0.87 with Vp=2.9 cm yr^{-1} (Table 1). Oblique subduction is indicated by the surface velocities near the dipping fault (Figure 11c).

In order to further understand the influence of faults on the oblique subduction, we now show two additional calculations of another configuration of slab and spreading center (Figure 11d for cases 19 and 20). In these two cases, the strike of the slab is parallel to that of the spreading center, but the transform faults are oblique to both the slab and spreading center (Figure 11d). This configuration of faults and slab is not observed, but these two cases clearly show the physics of fault interaction. Again, for case 19 with no faults, surface velocity displays a large internal strain rate and does not show oblique subduction (i.e., the velocities are perpendicular to the strike of slab) (Figure 11e). However, when faults are included (case 20), plate-like features including oblique subduction and uniform surface velocities emerge (Figure 11f).

3.3. Discussions

Studies of earthquakes show that most strain in subduction zones is accomplished through thrust faulting [*Davies and Brune*, 1971; *Kanamori*, 1977; *Ruff and Kanamori*, 1983], while some strain is released through normal faulting within subducting lithosphere [*Kikuchi and Kanamori*, 1995]. Our 2-D model with a preexisting dipping fault and a stress-weakening rheology with n=3 (case 2) is consistent with these observed features of strain and stress. The relative motion across the dipping fault is about the same as the converging velocity between the subducting and overriding plates (Figure 5d), consistent with observations [*Davies and Brune*, 1971; *Ruff and Kanamori*, 1983]. In the subducting plate and below the dipping fault, there is significant strain and the principal stress is perpendicular to the fault (Figure 5e), consistent with observations of normal fault earthquakes [*Kikuchi and Kanamori*, 1995]. Our models of dynamic compensation of the slabs beneath a dipping fault are consistent with outer rise and trench topography (Figure 4d) [*Zhong and Gurnis*, 1994b]. The excess depression in the back arc region evident in the model (Figure 4d) indicates that other processes, perhaps volcanism, may have significant influence on dynamic topography.

Subduction zone structure is difficult to be reproduced in models with a purely instantaneous stress-weakening rheology with no fault (cases 1, 4 and 5). However, lithospheric weakening above the slab may give rise to realistic plate velocities, especially if a pseudo-plastic rheology is used (Figure 4b). Without a fault, the maximum deviatoric stress (and strain rate) in the lithosphere always occurs in the overriding plate and directly above the slab, independent of the exponent n and yield stress (Figures 3e, 6b, and 6d). This is because the stress is primarily determined by the slab buoyancy. With stress-weakening rheology, either n=3 or our pseudo-plastic rheology, the maximum stress will weaken the region directly above the slab and produce a weak margin (Figures 3 and 6). The surface location of this margin depends on the geometry of slab and moves further towards the overriding plate for a shallower slab dip (Figure 6). This is inconsistent with the observation that converging margins tend to move more towards oceanic plates with respect to the location of slabs when the subduction dip becomes smaller [*Jarrard*, 1986]. Moreover, the stress and strain rate fields from these models (Figures 3 and 6 for cases 1, 4 and 5) are very different from the model with a fault (Figure 5 for case 2) and cannot explain observed features. These models suggest that the stress weakening rheology may not be the primary cause for the observed stress and strain patterns in subduction zones.

The 3-D models show that the interaction between a power-law rheology and weak faults produces the basic features of plate tectonics including small internal strain and significant toroidal motion. The models suggest that faults are probably weak, consistent with other inferences [*Lachenbruch and Sass*, 1988; *Bird*, 1978]. Weak faults alone may not be sufficient to produce plate-like surface motion and the stress-weakening rheology clearly plays a fundamental role, but the nonlinearity need not be strong. A weak coupling between the lithosphere and the upper mantle is also required to produce plate-like surface motion, suggesting that the upper mantle viscosity should be much smaller than the lithosphere. This seems to be compatible with the viscosity structure constrained by the Earth's geoid [*Hager and Richards*, 1989; *Hager and Clayton*, 1989]. However, some other inversion results from the geoid suggest a relatively strong upper mantle (from a depth of 100 km to 410 km) [e.g., *King and Masters*, 1992]. Increasing fault strength (i.e., the horizontal coupling between plates) reduces the ratio of toroidal to poloidal motion and increases.

the internal strain, while the viscosity contrast between the lithosphere and upper mantle (i.e., the vertical coupling) only influences the distribution of strain. This suggests that both the strain pattern and ratio of toroidal to poloidal motion are important in characterizing plate motion [*Bercovici*, 1995; *Zhong and Gurnis*, 1996].

Faults strongly influence the direction of plate motion. A transform fault tends to enhance plate motion along its strike; a dipping fault decouples subducting from overriding plates. Therefore the incorporation of these faults results in oblique subduction when the strike of transform faults is nonperpendicular to the strike of subducted slabs (Figures 8 and 9). The influences of transform faults on plate motion revealed from our models are consistent with some inference based on plate kinematics [*Richards and Engebreson*, 1994].

As we have shown, the interaction between preexisting weak faults and power law rheology produces the observed pattern of plate motion in instantaneous mantle flow models. Essentially, our models indicate the importance of the heterogeneity in lithospheric strength (i.e., weak faults versus surrounding media) to the observed plate motion. On the basis of the observations of surface stress and strain and our numerical models, we suggest that the instantaneous stress-weakening rheology may not be the primary cause for producing such heterogeneity in lithospheric strength. We think that this heterogeneity in lithospheric strength is likely an integrated effect of lithospheric deformation over geologic time, and lithospheric deformation history, instantaneous stress-weakening, and lithology may all contribute to the development of this heterogeneity. Initial attempts have been made in incorporating deformation history [*Sleep*, 1997] and self-lubrication mechanism based on void generation and volatile ingestion [*Bercovici*, 1998] into lithospheric rheology models, but it remains a challenging question as to how different processes contribute to the development of this heterogeneity.

4. Conclusions

On the basis of observations and numerical models, we argue that fault decoupling at plate margins primarily results from history-dependent lithospheric deformation rather than from instantaneous stress-weakening rheology. We suggest that faults should be treated as preexisting mechanical structure for instantaneous mantle flow models. With models incorporating preexisting faults, a power-law rheology (n=3), and realistic buoyancy forces including slab pull and ridge push forces, we have demonstrated that nonlinear interaction between weak faults and a power-law rheology explains a number of key features of plate motion, such as concentrated strain within plate margins and a significant toroidal component.

Our models show that in order to produce plate-like motion, both the frictional stress on faults and the viscosity in the upper mantle immediately below the lithosphere (i.e., asthenosphere) are required to be small. Both the plateness and ratio of toroidal to poloidal velocities are reduced with increased fault coupling. Plateness is sensitive to the viscosity contrast between the lithosphere and upper mantle and is reduced as the viscosity contrast is decreased. However, the viscosity contrast does not significantly influence the ratio of toroidal to poloidal velocities. Therefore both the plateness and ratio of toroidal to poloidal velocities are necessary in characterizing plate motion.

Our models show that weak transform faults enhance surface motion in the direction parallel to the strikes of transform faults. That is, transform faults appear to guide plate motion. This guiding influence and the decoupling of thrust faults may result in oblique subduction where the strike of subducted slabs is oblique to transform fault. Our subduction zone models with a dipping fault also produce short-wavelength features including oceanic trench and forebulge topography and principal stresses that are largely consistent with subduction zone observations.

Appendix A: Incorporation of Fault Planes Into 3D Finite Element Models

Constrained elements and matrix transformation are used to incorporate faults into 3-D finite element models. These techniques are similar to those by *Melosh and Williams* [1989] and *Barr and Houseman* [1996] and are an extension of our previous penalty function method [*Zhong and Gurnis*, 1994b]. The general treatment for such problems is given by Cook [1981] and will be briefly described as follows.

Fault planes consist of elemental boundaries (Figure A1a). Those elements with boundaries which overlap a fault are called constrained elements. The constraints on faults are that velocities are continuous in the normal direction $\vec{n}=(n_1,n_2,n_3)$, while tangential velocities are coupled with a specified frictional stress, where $\vec{n}$ is defined in a global coordinate system x, y, and z (Figure A1a). We define two

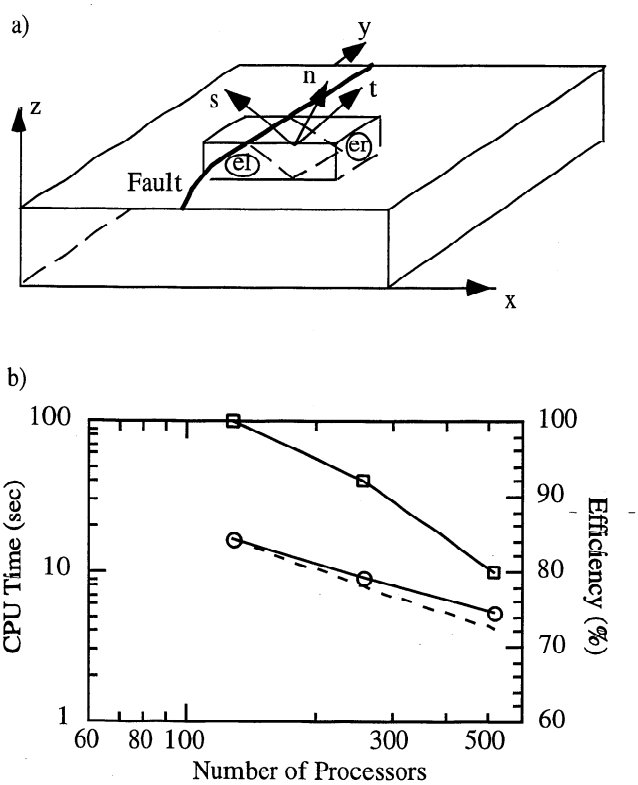

Figure A1. (a) Three dimensional fault with constrained elements in both global (x, y, z) and local (n, t, s) coordinate systems. (b) CPU time and efficiency versus the number of processors for the parallelized 3D finite element software Citcom on the Intel Paragon with 512 processors. For the benchmark in Figure A1b, the CPU times are only for solution of inner loop iteration of velocity and mesh size is 160x64x80.

tangential directional vectors $\vec{t}=(t_1,t_2,t_3)$ and $\vec{s}=(s_1,s_2,s_3)$ such that $\vec{n}$, $\vec{s}$, and $\vec{t}$ form an orthogonal coordinate system (i.e., local coordinate system) (Figure A1a). We may define such a local coordinate system for each faulted node within constrained elements.

For each constrained element, elemental matrix equations in the global coordinate system are

$$KU+G^TP=F, \tag{A1}$$

$$GU=0, \tag{A2}$$

where K is a stiffness matrix with 24x24 entries (this is for a 3-D trilinear element with eight nodes); F and G^T are force and divergence vectors; P is the pressure which is constant within the element; $U'=(.,.,.,u_x^i,u_y^i,u_z^i,.,.,.)^T$ where i is the local node index. If local node i is a faulted node, we will use velocities in the local coordinate system for this node, and this can be done through the following transformation: $U'=\Gamma_i U$, where $U'=(.,.,.,u_n^i,u_t^i,u_s^i,.,.,.)^T$ is the new velocity vector; Γ_i is a transformational matrix with 24x24 entries with only nonzero entries in eight 3x3 submatrices on the diagonal of Γ_i. Seven of the eight 3x3 submatrices are unit matrices, and the only nonunit submatrix T_i is associated with node i. T_i can be written as

$$T_i=\begin{bmatrix} n_1 & n_2 & n_3 \\ t_1 & t_2 & t_3 \\ s_1 & s_2 & s_3 \end{bmatrix}. \tag{A3}$$

Applying the transformation to equations (A1) and (A2) leads to

$$\Gamma_i K\Gamma_i^T U' + \Gamma_i G^T P = \Gamma_i F, \tag{A4}$$

$$G\Gamma_i^T U' = 0. \tag{A5}$$

If we define $K'=\Gamma_i K\Gamma_i^T$, which remains symmetric and positive definite, $G'=G\Gamma_i^T$, and $F'=\Gamma_i F$, then the form of (A4) and (A5) are identical to (A1) and (A2). If there are other faulted nodes within this element, we consecutively apply this transformation to these nodes such that velocities associated with each faulted node in U' vector are based on the local coordinate system for that node.

Fault constraints are enforced when elemental matrix equations are assembled into global matrix equations. For each faulted node in the global matrix equations, we assign five degrees of freedom: one normal velocity, u_n^i, and four tangential velocities, ${}_lu_t^i$, ${}_lu_s^i$, ${}_ru_t^i$, and ${}_ru_s^i$, with the first two for the left side of the fault and the last two for the right (Figure A1a). The parameters ${}_lu_t^i$ and ${}_lu_s^i$, and ${}_ru_t^i$ and ${}_ru_s^i$ are used for the constained elements on the left and right sides of the fault, respectively. After the global equations are solved, we obtain the velocity field in which the velocities on faulted nodes are based on the local coordinate system for each faulted node. We can apply the transformation $U=\Gamma_i^T U'$ for each faulted node to retrieve the velocities in the global coordinate system.

Appendix B: Parallelization of 3D Finite Element Code Citcom With MPI

Parallel computing has been previously used in modeling mantle dynamics [*Gurnis et al.*, 1988; *Tackley*, 1994; *Bunge and Baumgardner*, 1995]. *Tackley* [1994] used a message passing software native to a massively parallel processing supercomputer Intel Delta for a finite volume code and a spectral convection code [*Glatzmaier*, 1988], while *Bunge and Baumgardner* [1995] parallelized a finite element code [*Baumgardner*, 1985] with a message passing software PVM. In the last few years, as a result of steady improvement of both interprocessor communication speed and message passing softwares, parallel computing has become very effective.

We have applied Message Passing Interface software MPI [*Snir et al.*, 1996] to parallelize the finite element code Citcom [*Moresi and Solomatov*, 1995; *Moresi and Gurnis*, 1996]. Since MPI is widely supported on many different parallel computers, including shared and distributed memory machines, the parallelized Citcom can be easily ported onto different parallel computers. The two-level Uzawa algorithm implemented in Citcom displays a significant locality and is suitable for parallelization. Computations of stiffness matrix, force vectors, and divergence, gradient, and Laplacian operators are performed at an element level and do not involve interprocessor communication. Communications are needed in computing global residue terms and assembling force vectors. Communications only involve information on boundaries of each computational domain. The parallelized Citcom achieves better than 80% efficiency on the massively parallel processing supercomputer Intel Paragon for a moderate size problem (Figure A1b).

Acknowledgments. This work is supported by the David and Lucile Packard Foundation and NSF grant EAR-9417645. We thank Hiroo Kanamori for many enlightening discussions and David Bercovici and Paul Tackley for reviewing the paper. Some of the calculations were carried out on the Intel Paragon supercomputer at Caltech's Center for Advanced Computer Research. This is contribution 6204 of the Division of Geological and Planetary Sciences, California Institute of Technology.

References

Artyushkov, E. V., Stresses in the lithosphere caused by crustal thickness inhomogeneities, *J. Geophys. Res.*, *78*, 7675-7708, 1973.

Barr, T. D., and G. A. Houseman, Distribution of deformation around a fault in a nonlinear ductile medium, *Geophys. Res. Lett.*, *19*, 1145-1148, 1992.

Barr, T. D., and G. A. Houseman, Deformation fields around a fault embedded in a nonlinear ductile medium, *Geophys. J. Int.*, *125*, 473-490, 1996.

Baumgardner, J. R., Three dimensional treatment of convection flow in the Earth's mantle, *J. Stat. Phys.*, *39*, Nos 5/6. 501-511, 1985.

Bercovici, D., A simple model of plate generation from mantle flow, *Geophys. J. Int.*, *114*, 635-650, 1993.

Bercovici, D., A source-sink model of the generation of plate tectonics from non-Newtonian mantle flow, *J. Geophys. Res.*, *100*, 2013-2030, 1995.

Bercovici, D., Generation of plate tectonics from lithosphere-mantle flow and void-volatile self-lubrication, *Earth Planet. Sci. Lett.*, in press, 1998.

Bird, P., Stress and temperature in subduction shear zones: Tonga and Mariana, *Geophys. J. Roy. Astron. Soc.*, *55*, 411-434, 1978.

Bird, P., and X. H. Kong, Computer-simulations of California tectonics confirm very low strength of major faults, *Geol. Soc. Am. Bull.*, *106*, 159-174, 1994.

Bunge, H.-P., and J. R. Baumgardner, Mantle convection modeling on parallel virtual machines, *Comput. in Phys.*, *9*, No 2, 207-215, 1995.

Christensen, U. R., Convection in a variable-viscosity fluid: Newtonian versus power-law rheology, *Earth Planet. Sci. Lett.*, *64*, 153-162, 1983.

Christensen, U. R., and H. Harder, 3-D convection with variable viscosity, *Geophys. J. Int.*, *104*, 213-226, 1991.

Cook, R. D., *Concepts and Application of Finite Element Analysis*, 2nd ed., 537 pp., John Wiley, New York, 1981

Davies, G. F., Role of the lithosphere in mantle convection, *J. Geophys. Res.*, *93*, 10451-10466, 1988.

Davies, G. F., Mantle convection model with a dynamic plate: topography, heat flow and gravity anomalies, *Geophys. J. Int.*, *98*, 461-464, 1989.

Davies, G. F., and J. N. Brune, Regional and global fault slip rates from seismicity, *Nature*, *229*, 101-107, 1971.

Forsyth, D. W. and S. Uyeda, On the relative importance of the driving forces of plate motion, *Geophys. J. R. Astron. Soc.*, *43*, 163-200, 1975.

Gable C. W., R. J. O'Connell, and B. J. Travis, Convection in three dimensions with surface plates: Generation of toroidal flow, *J. Geophys. Res.*, *96*, 7205-7223, 1991.

Glatzmaier, G. A., Numerical simulations of mantle convection: time-dependent, three-dimensional, compressible, spherical shell, *Geophys. Astrophys. Fluid Dyn.*, *43*, 223-264, 1988.

Gurnis, M., Large-scale mantle convection and the aggregation and dispersal of supercontinents, *Nature*, *332*, 695-699, 1988.

Gurnis, M., Generation of plate tectonics from mantle convection, paper presented at Chapman Conference on the History and Dynamics of Global Plate Motions, AGU, Pacific Grove, Calif., 1997.

Gurnis, M. and B. H. Hager, Controls on the structure of subducted slabs, *Nature, 335,* 317-322, 1988.

Gurnis, M., A. Raefsky, G. A. Lyzenga, and B. H. Hager, Finite element solution of thermal convection on a hypercube concurrent computer, in *Proceedings of Third Conference on Hypercube Concurrent Computers and Applications*, edited by G. C. Fox, 1176-1179, Assoc. of Comp. Mach., New York, 1988.

Gurnis, M., C. Eloy, and S. Zhong, Free-surface formulation of mantle convection - II. Implication for subduction-zone observables, *Geophys. J. Int.*, *127*, 719-727, 1996.

Hager, B. H., and R. W. Clayton, Constraints on the structure of mantle convection using seismic observations, flow models, and the geoid, in *Mantle Convection*, ed. by R. W. Peltier, pp. 657-763, Gordon and Breach, Newark, N.J., 1989.

Hager, B. H., and R. J. O'Connell, Kinematic models of large-scale flow in the Earth's mantle, J. Geophys. Res., *84*, 1031-1048, 1979.

Hager, B. H., and R. J. O'Connell, A simple global model of plate dynamics and mantle convection, *J. Geophys. Res.,, 86*, 4843-4867, 1981.

Hager, B. H., and M. A. Richards, Long-wavelength variations in Earth's geoid: physical models and dynamical implications, *Philos. Trans. R. Soc. London*; Ser. A *328*, 309-327, 1989.

Jacoby, W. R. and H. Schmeling, On the effects of the lithosphere on mantle convection and evolution, *Phys. Earth Planet. Inter.*, *29*, 305-319, 1982.

Jaeger, J. C., *Elasticity, Fracture and Flow*, 3rd edition, Methuen, New York, 1969.

Jarrad, R. D., Relations among subduction parameters, *Rev. Geophys., 24*, 217-284, 1986.

Jeffreys, H., *The Earth*, Cambridge Univ. Press, New York, 1970.

Kanamori, H., The energy release in great earthquakes, *J. Geophys. Res.*, *82*, 2981-2987, 1977.

Kanamori, H., The state of stress in the Earth's lithosphere, in *Physics of the Earth's Interior*, edited by A. Dziewonski and E. Boschi, pp. 531-554, Amsterdam, North-Holland, 1980.

Kapitzke, U., Finite element convection models: comparison of shallow and deep mantle convection, and temperatures in the mantle, *J. Geophys., 46*, 97-121, 1979.

Karato, S., and P. Wu, Rheology of the upper mantle: A synthesis, *Science, 260*, 771-778, 1993.

Kikuchi, M., and H. Kanamori, The Shikotan earthquake of October 4, 1994: Lithospheric earthquake, *Geophys. Res. Lett., 22*, 1025-1028, 1995.

King S. D., and B. H. Hager, The relationship between plate velocity and trench viscosity in Newtonian and power-law subduction calculations, *Geophys. Res. Lett., 17*, 2409-2412, 1990.

King, S. D. and G. Masters, An inversion for radial viscosity structure using seismic tomography, *Geophys. Res. Lett, 19*, 1551-1554, 1992.

Lachenbruch, A. H., and J. H., Sass, The stress heat-flow paradox and thermal results from Cajon Pass, *Geophys. Res. Lett., 15*, 981-984, 1988.

Lenardic, A., and W. M. Kaula, Self-lubricated mantle convection -- two-dimensional models, *Geophys. Res. Lett., 21*, 1707-1710, 1994.

Lithgow-Bertelloni, C. and M. A. Richards, Cenozoic plate driving forces, *Geophys. Res. Lett., 22*, 1317-1320, 1995.

Melosh, H. J., and C. A. Williams, Jr., Mechanics of graben formation in crustal rocks: a finite element analysis, *J. Geophys. Res., 94*, 13,961-13,973, 1989.

Moresi, L. N., and M. Gurnis, Constraints on the lateral strength of slabs from three dimensional dynamic flow models, *Earth Planet. Sci. Lett., 138*, 15-28, 1996.

Moresi, L. N., and V. S. Solomatov, Numerical investigation of two dimensional convection with extremely large viscosity variations, *Phys. Fluids, 9*, 2154-2162, 1995.

Morgan, J. W., Rises, trenches, great faults, and crustal blocks, *J. Geophys. Res., 73*, 1959-1982, 1968.

Olson, P., and D. Bercovici, On the equipartition of kinetic-energy in plate tectonics, *Geophys. Res. Lett., 18*, 1751-1754, 1991.

Puster, P., B. H. Hager, and T. H. Jordan, Mantle convection experiments with evolving plates, *Geophys. Res. Lett., 22*, 2223-2226, 1995.

Ricard, Y. and C. Vigny, Mantle dynamics with induced plate tectonics, *J. Geophys. Res., 94*, 17543-17559, 1989.

Richards, M. A., and D. C. Engebreson, Transform faults – A guiding force of plate tectonics, *Eos Trans. AGU, 75* (16), Spring Meet. Suppl., 64, 1994.

Ruff, L. J., and H. Kanamori, Seismic coupling and uncoupling at subduction zones, *Tectonophysics*, *99*, 99-117, 1983.

Schmeling, H., and W. R. Jacoby, On modelling the lithosphere in mantle convection with nonlinear rheology, *J. Geophys., 50*, 89-100, 1981.

Sleep, N. H., Stress and flow beneath island arcs, *Geophys. J. R. Astron. Soc., 42*, 827-857, 1975.

Sleep, N. H., Application of a unified rate and state friction theory to the mechanics of fault zones with strain localization, *J. Geophys. Res., 102*, 2875-2895, 1997.

Snir, M., S. W. Otto, S. Huss-Lederman, D. W. Walker, and J. Dongarra, *MPI: The Complete Reference*, 336, MIT Press, Cambridge, Mass., 1996.

Solomatov, V. S., and L. Moresi, Why does earth have plate tectonics?, paper presented at Chapman Conference on the History and Dynamics of Global Plate Motions, AGU, Pacific Grove, Calif., 1997.

Tackley, P. J., Three-dimensional models of mantle convection: Influence of phase transitions on temperature-dependent viscosity, Ph.D. thesis, Calif. Inst. of Technol., Pasadena, 1994.

Tackley, P. J., Self-consistent generation of tectonic plates in three-dimensional mantle convection, *Earth Planet. Sci. Lett.*, in press, 1998.

Tichelaar, B., and L. J. Ruff, Depth of seismic coupling along subduction zones, *J. Geophys. Res., 98*, 2017-2037, 1993.

Vassiliou, M. S., and B. H. Hager, Subduction zone earthquakes and stress in slabs, *Pure Appl. Geophys., 128*, 547-624, 1988.

Weinstein, S. A., Thermal convection in a cylindrical annulus with a non-Newtonian outer surface, *Pure Appl. Geophys., 146*, 551-572, 1996.

Weinstein, S. A., and P. Olson, Thermal convection with non-Newtonian plates, *Geophys. J. Int., 111*, 515-530, 1992.

Wilson, J. T., A new class of faults and their bearing on continental drift, *Nature, 207*, 343-347, 1965.

Zhong, S., and M. Gurnis, The role of plates and temperature-dependent viscosity in phase change dynamics, *J. Geophys. Res., 99*, 15,903-15,917, 1994a.

Zhong, S., and M. Gurnis, Controls on trench topography from dynamic models of subducted slabs, *J. Geophys. Res., 99*, 15,683-15,695, 1994b.

Zhong, S., and M. Gurnis, Mantle convection with plates and mobile, faulted plate margins, *Science, 267*, 838-843, 1995.

Zhong, S., and M. Gurnis, Interaction of weak faults and non-Newtonian rheology produces plate tectonics in a 3-D model of mantle flow, *Nature, 383*, 245-247, 1996.

M. Gurnis, Seismological Laboratory, 252-21, California Institute of Technology, Pasadena, CA 91125. (e-mail: gurnis@gps.caltech.edu)

L. Moresi, CSIRO Exploration and Mining, 39 Fairway, Nedlands, WA 6009, Australia. (e-mail: louis@ned.dem.csiro.au)

S. Zhong, Department of Earth, Atmospheric, and Planetary Sciences, Massachusetts Institute of Technology, Bldg E54-511, Cambridge, MA 02139. (e-mail: szhong@rayleigh.mit.edu)

(Received August 4, 1997; revised February 1, 1998;
accepted February 12, 1998.)